Dalton Transactions

PAPER

Cite this: *Dalton Trans.*, 2016, **45**, 16471

First quadruple-glycine bridging mono-lanthanide-substituted borotungstate hybrids†

Jiancai Liu,[a] Jing Yu,[a] Qing Han,[a] Yue Wen,[a] Lijuan Chen*[a] and Junwei Zhao*[a,b]

A class of novel organic–inorganic hybrid lanthanide (Ln)-substituted Keggin-type borotungstates $K_4Na_4H_4[Ln_2(gly)_4(\alpha\text{-}BW_{11}O_{39})_2]\cdot 23H_2O$ [Ln = Ce^{3+} (**1**), Pr^{3+} (**2**), Nd^{3+} (**3**), Sm^{3+} (**4**), Eu^{3+} (**5**), Tm^{3+} (**6**); gly = glycine] have been synthesized from the reaction of $K_8[BW_{11}O_{39}H]\cdot 13H_2O$, $NaAc\cdot 6H_2O$ and $Ln(NO_3)_3\cdot 6H_2O$ by employing gly ligands as structure-stabilizing agents in the conventional aqueous solution system and structurally characterized by elemental analyses, IR spectroscopy, thermogravimetric (TG) analyses, powder X-ray diffraction (PXRD) and single-crystal X-ray diffraction. The common prominent structural feature of isomorphic **1–6** is that all of them consist of two mono-Ln-substituted Keggin $[Ln(\alpha\text{-}BW_{11}O_{39})]^{6-}$ fragments linked by four gly ligands, furnishing an intriguing dimeric assembly of the quadruple-gly-connective mono-Ln-substituted borotungstate, in which each carboxylic oxygen atom from gly ligands is bound to Ln^{3+} cations in the μ_2-O or μ_3-O mode. To the best of our knowledge, **1–6** represent the first examples of inorganic–organic hybrid Ln-substituted borotungstates functionalized by quadruple amino acid bridges. The solid-state photoluminescence properties of **3–5** have been determined at ambient temperature and the photoluminescence emission spectra exhibit the characteristic emission bands derived from Ln^{3+} centers. The thermostability of **1–6** has been studied and the thermal decomposition procedure of **3** has been comprehensively investigated with the assistance of variable-temperature PXRD patterns and variable-temperature IR spectra. Furthermore, magnetic susceptibility measurements of **1**, **2** and **4** have been conducted.

Received 8th August 2016,
Accepted 13th September 2016

DOI: 10.1039/c6dt03148j

www.rsc.org/dalton

Introduction

Polyoxometalates (POMs) are early transition-metal oxide anion clusters constructed from transition metals in their high oxidation states (primarily Mo^{VI}, W^{VI}, V^{V}, Nb^{V} and Ta^{IV}); they exhibit unrivalled structural diversities, attractive properties and potential applications in catalysis, magnetism, medicine, materials science and nanotechnology.[1] In particular, polyoxotungstates (POTs), as a large subclass of POM chemistry, are always utilized as multifunctional inorganic polydentate O-donor candidates to accommodate oxophilic d- or f-block metals for the construction of transition metal (TM) or Ln substituted POTs on account of their highly negatively charged and O-enriched surface. Hitherto, a tremendous number of TM-substituted POTs have been discovered ever since the first example was addressed by Simmons in 1962 and its structure that was composed of an 11-tungstosilicate wherein one W atom of the Keggin structure was replaced by a Co^{2+} ion was determined by St. Moritz in 1966.[2] In contrast, the development of Ln-substituted POTs (LSPs) is relatively laggard. Historically, in 1914, Barbieri initiated the study of the reaction of polyoxoanions and Ln^{3+} ions with the discovery of the first Ln-substituted POM $(NH_4)_2[H_6CeMo_{12}O_{42}]\cdot nH_2O$,[3] and after a long-standing sluggish period, in 1971 Peacock and Weakley succeeded in obtaining a series of LSPs $[Ln(W_5O_{18})_2]^{n-}$ and synchronously explored the reactivity of $Ln^{3+/4+}$ cations with monolacunary Keggin-type $[XW_{11}O_{39}]^{n-}$ (X = Si^{IV}, P^{V}) and Dawson-type $[P_2W_{17}O_{61}]^{10-}$ polyoxoanions, giving rise to 1 : 1- or 1 : 2-type Keggin or Dawson LSPs.[4] These preliminary discoveries are undoubtedly extremely significant pioneering work, and not only shed light on the great possibilities in implanting Ln^{3+}cations into various POT precursors, but also pave the way for discovering neoteric LSPs.

[a]*Henan Key Laboratory of Polyoxometalate Chemistry, Institute of Molecular and Crystal Engineering, College of Chemistry and Chemical Engineering, Henan University, Kaifeng, Henan 475004, P. R. China. E-mail: ljchen@henu.edu.cn, zhaojunwei@henu.edu.cn*

[b]*State Key Laboratory of Structural Chemistry, Fujian Institute of Research on the Structure of Matter, Chinese Academy of Sciences, Fuzhou, Fujian 350002, P. R. China*

†Electronic supplementary information (ESI) available: IR spectra of **1–6** and $K_8[\alpha\text{-}BW_{11}O_{39}H]\cdot 13H_2O$, PXRD patterns of **1–6** and related structural figures; luminescence emission spectra and decay curves of **3–5** and $K_8[\alpha\text{-}BW_{11}O_{39}H]\cdot 13H_2O$; TG curves of **1–6**, and the variable temperature and PXRD spectra of **3**; BVS calculations of W, B and Ln atoms in **1–6**. CCDC 1495658–1495663. For ESI and crystallographic data in CIF or other electronic format see DOI: 10.1039/c6dt03148j

Henceforth, numerous LSPs have been reported over the past few decades which possess aesthetic structures as well as potential applications such as magnetism, photoluminescence and catalysis.[5]

Among LSPs, organic-ligand-functionalized Ln-substituted lacunary Keggin- or Dawson-type POTs have also been investigated.[5d–v] Notably, the research on the incorporation of organic ligands into the Ln–POT system has aroused increasing interest in that organic linkers can somewhat facilitate the agglomeration of Ln^{3+} centers to form polynuclear species, which are principally concentrated on the overwhelming variety of carboxylate ligands from monocarboxylic components (acetate, nicotinic acid, pyridine-4-carboxylic acid) to multicarboxylic components (tartrate, pyridinedicarbocylic, citric acid);[5d–v] however, amino acid ligands have been hardly employed in this respect and only a few examples containing gly, alanine (ala) or proline (pro) have been reported to date.[6] For instance, in 2007, Wang *et al.* first obtained an unusual ala-decorated quadrimeric cryptand-type arsenotungstate $[Ce_4As_4W_{44}O_{151}(ala)_4(OH)_2(H_2O)_{10}]^{12-}$;[6a] afterwards, their group successfully synthesized a strand of 1-D chainlike aggregates $[Ln_6(H_2O)_x\{As_4W_{44}(OH)_2(pro)_2O_{151}\}]^{10-}$ (Ln = Tb^{3+}, Dy^{3+}, Nd^{3+}) built from the crown-shaped units $[Ln_4(H_2O)_x\{As_4W_{44}(OH)_2(pro)_2O_{151}\}]^{16-}$ that are stabilized by pro ligands linked by two extra hydrated Ln^{3+} cations.[6b] Noticeably, Boskovic's group conducted a set of research studies on the reactivity of Ln^{3+} cations with arsenotungstates in the presence of gly, affording a new family of gly-based LSPs such as the 1-D chain $[Dy_4As_2W_{22}O_{76}(H_2O)_{19}(C_2H_5NO_2)_2]^{2-}$ ($C_2H_5NO_2$ = glycine) as well as discrete tetrameric species $[As_4(YW_3)W_{44}Y_4O_{159}(gly)_8(H_2O)_{14}]^{9-}$ and $[Ln_4As_5W_{40}O_{144}(H_2O)_{10}(gly)_2]^{21-}$ (Ln = Gd^{3+}, Tb^{3+}, Dy^{3+}, Ho^{3+}, Y^{3+}).[6c–e] Naruke and coworkers also accelerated the development of gly-functionalized LSPs with attaining two chiral enantiopure complexes $K_{1.3}Na_{3.2}H_{6.5}[L\text{-}Pr(PW_{11}O_{39})_2]\cdot 8.3L\text{-}pro\cdot 21.5H_2O$ and $K_{1.3}Na_{3.2}H_{6.5}[D\text{-}Pr(PW_{11}O_{39})_2]\cdot 8.3D\text{-}pro\cdot 17H_2O$ using L- and D-pro as the chiral auxiliary agents.[6f] Very recently, our group made a pro-modified dimeric phosphotungstate, $KNa_3[HPro]_7[Sm(\alpha\text{-}PW_{11}O_{39})_2]\cdot Pro\cdot 18H_2O$, and characterized its ferroelectric behavior.[6g] Nevertheless, examples of Ln-substituted borotungstates (BTs) are not reported as extensively as phosphotungstates or arsenotungstates.[5k,7] Some inchoate reports have emerged with the discovery of 1 : 1-type complexes $[Ln(BW_{11}O_{39})(H_2O)_3]^{6-}$ (Ln = Sm^{3+}, Eu^{3+}, Tb^{3+}, Dy^{3+}) as well as 1 : 2-type complexes $[Ln(BW_{11}O_{39})_2]^{15-}$ and $[Ln(BW_{11}O_{39})(W_5O_{18})]^{12-}$ (Ln = Ce^{3+}, Eu^{3+}).[7a–d] Furthermore, some extended structures from 1-D $[Ce_2(BW_{11}O_{39})_2(H_2O)_6]^{12-}$ and $\{[Ho_4(dpdo)_8(H_2O)_{16}BW_{12}O_{40}](H_2O)_2\}^{7+}$ (dpdo = 4,4′-bipyridine-*N*,*N*′-dioxide hydrate)[7e,f] to 3-D $[LnK(H_2O)_{12}][Ln(H_2O)_6]_2[(H_2O)_4LnBW_{11}O_{39}\ H]_2\cdot 20H_2O$ (Ln = Ce^{3+}, Nd^{3+}) and $\{[(C_6NO_2H_5)Ln(H_2O)_5]_2[(H_2O)_4\ LnBW_{11}O_{39}H]_2\}^{4-}$ (Ln = Ce^{3+}, Nd^{3+}, $C_6NO_2H_5$ = pyridine-4-carboxylic acid) were also resoundingly separated.[5k] These sporadic examples not only hint at the great difficulty and challenge in preparing novel Ln-substituted BTs (LSBs), but also pave the way for discovering other BT-based functional materials.

As far as we know, BTs delegate a category of species with unusual properties in comparison with the common silicotungstate and phosphotungstate analogues,[8] partly because B^{III} heteroatoms having the lowest charge and the smallest size can probably define some distinctive properties,[9] and the electron-deficient B^{III} atoms can adopt either trigonal or tetrahedral coordination modes.[10] These unique features inspired us to gain a close insight into them. Considering that no examples of LSBs containing amino acid ligands have been reported to date, it was of particular interest for us to explore an appropriate approach to introduce amino acid ligands and various Ln^{3+} cations into the BT system for obtaining a myriad of manifold LSBs with diverse functionalities. It is well known that Ln^{3+} ions behaving as hard acids with high coordination numbers and strong oxophilic characteristics are prone to coalesce with oxygenic ligands such as POM frameworks, and their fascinating photophysical and magnetic properties make them popular in the aspect of potential applications. What's more, amino acid ligands have flexible carboxyl and amino coordination sites and the inclusion of them can bridge and stabilize the final structures, whilst the *in situ* assembly of lacunary POT precursor under conventional aqueous conditions has been developed as an efficient and ubiquitous method for constructing novel LSPs. On the basis of these considerations, we launched the exploration of assembly reactions of BT precursors with Ln^{3+} cations in the presence of amino acid ligands and thus a family of quadruple-gly bridging LSBs $K_4Na_4H_4[Ln_2(gly)_4(\alpha\text{-}BW_{11}O_{39})_2]\cdot 23H_2O$ [Ln = Ce^{3+} (**1**), Pr^{3+} (**2**), Nd^{3+} (**3**), Sm^{3+} (**4**), Eu^{3+} (**5**), Tm^{3+} (**6**); gly = glycine] were obtained, delegating the first examples of inorganic–organic hybrid BTs based on Ln^{3+} cations and amino acid linkers. Furthermore, the photoluminescence (PL) properties and lifetime decay behaviors of **3–5** have been studied, indicating that their PL behaviors are mainly derived from the characteristic emissions from Ln^{3+} centers. The lifetime of **4** originates from the combined action of Ln^{3+} cations and BT segments whereas the lifetimes of **3** and **5** chiefly originate from Ln^{3+} cations. The magnetic measurements of **1**, **2** and **4** have been performed between 1.8 and 300 K. The declining of $\chi_M T$ values of **1** and **4** with decreasing temperature can principally be due to the antiferromagnetic couplings interactions within magnetic centers as well as the thermal depopulation of the Stark levels, whereas the magnetic behavior of **2** may be primarily ascribed to the thermal progressive depopulation of the Stark levels of Pr^{3+} ions. In addition, TG analyses of **1–6** have been performed and the thermal decomposition process of **3** has been intensively investigated by multiple dynamic analyses including TG curves, variable-temperature PXRD patterns and variable-temperature IR spectra.

Experimental

Materials and physical measurements

The precursor $K_8[\alpha\text{-}BW_{11}O_{39}H]\cdot 13H_2O$ was synthesized according to a literature method[9a] and characterized by IR

spectroscopy. All other chemicals were used as purchased without further purification. C, H and N elemental analyses were conducted using a Perkin-Elmer 2400-II CHNS/O analyzer. Inductively coupled plasma atomic emission spectrometry (ICP-AES) was performed using a Perkin-Elmer Optima 2000 ICP-AES spectrometer. IR spectra were recorded on a Bruker Vertex 70 IR spectrometer using KBr pellets in the range of 4000–400 cm^{-1}. PXRD patterns were collected on a Bruker AXS D8 Advance diffractometer instrument with Cu Kα radiation (λ = 1.54056 Å) at 293 K. TG analyses were performed using a Mettler–Toledo TGA/SDTA 851e instrument under a N_2 atmosphere with a heating rate of 10 °C min^{-1} from 25 to 800 °C. The magnetic experiments were carried out using a Quantum Design SQUID (MPMS-XL 7). PL spectra, lifetime decay behaviors and luminescence quantum yields were obtained in the solid state at ambient temperature using an Edinburgh FLS 980 Analytical Instrument equipped with a 450 W xenon lamp and a μF900H high-energy microsecond flash lamp as the excitation source.

Preparations of 1–6

$K_4Na_4H_4[Ce_2(gly)_4(\alpha\text{-}BW_{11}O_{39})_2]\cdot 23H_2O$ (1). $K_8[\alpha\text{-}BW_{11}O_{39}H]\cdot 13\ H_2O$ (3.006 g, 0.938 mmol) and $NaAc\cdot 3H_2O$ (0.525 g, 3.858 mmol) were dissolved in 20 mL distilled water under stirring and the pH of the solution was adjusted to 2.7 by 6 mol L^{-1} HCl. After the solution was stirred for *ca*. 20 min, $Ce(NO_3)_3\cdot 6H_2O$ (0.207 g, 0.477 mmol) and gly (0.196 g, 2.610 mmol) were successively added and the pH value was adjusted to 2.7 again by using 6 mol L^{-1} NaOH. The resulting solution was stirred for another 30 min, kept in a 90 °C water bath for 2 h and filtered when it had cooled to room temperature. Slow evaporation of the filtrate at room temperature led to yellow needle-like crystals of **1** in about two weeks. Yield: 0.37 g (23.3%) based on $Ce(NO_3)_3\cdot 6H_2O$. Elemental analysis (%) calcd: C, 1.46; H, 1.07; N, 0.85; Na, 1.40; K, 2.38; W, 61.64; Ce, 4.27. Found: C, 1.35; H, 1.17; N, 0.76; Na, 1.62; K, 2.21; W, 61.50; Ce, 4.39. IR (KBr, cm^{-1}): 3418(s), 1621(m), 1477(m), 1416(w), 948(m), 822(s), 691(w), 523(m), 427(w) (Fig. S1†).

$K_4Na_4H_4[Pr_2(gly)_4(\alpha\text{-}BW_{11}O_{39})_2]\cdot 23H_2O$ (2). The synthetic procedure of **2** is similar to **1** except that $Ce(NO_3)_3\cdot 6H_2O$ (0.207 g, 0.477 mmol) was replaced by $Pr(NO_3)_3\cdot 6H_2O$ (0.207 g, 0.477 mmol). Green needle-like crystals of **2** were obtained. Yield: 0.32 g (20.1%) based on $Pr(NO_3)_3\cdot 6H_2O$. Elemental analysis (%) calcd: C, 1.46; H, 1.07; N, 0.85; Na, 1.40; K, 2.38; W, 61.63; Pr, 4.29. Found: C, 1.43; H, 1.18; N, 0.74; Na, 1.55; K, 2.24; W, 61.75; Pr, 4.18. IR (KBr, cm^{-1}): 3410(s), 1621(m), 1469(m), 1414(w), 947(m), 819(s), 691(w), 517(m), 428(w) (Fig. S1†).

$K_4Na_4H_4[Nd_2(gly)_4(\alpha\text{-}BW_{11}O_{39})_2]\cdot 23H_2O$ (3). The synthetic procedure of **3** is similar to **1** except that $Ce(NO_3)_3\cdot 6H_2O$ (0.207 g, 0.477 mmol) was replaced by $Nd(NO_3)_3\cdot 6H_2O$ (0.207 g, 0.472 mmol). Purple needle-like crystals of **3** were obtained. Yield: 0.41 g (25.8%) based on $Nd(NO_3)_3\cdot 6H_2O$. Elemental analysis (%) calcd: C, 1.46; H, 1.07; N, 0.85; Na, 1.40; K, 2.38; W, 61.56; Nd, 4.39. Found: C, 1.51; H, 1.10; N, 0.78; Na, 1.61; K, 2.21; W, 61.47; Nd, 4.49. IR (KBr, cm^{-1}): 3433(s), 1645(m), 1476(m), 1412(w), 946(m), 819(s), 697(w), 518(m), 430(w) (Fig. S1†).

$K_4Na_4H_4[Sm_2(gly)_4(\alpha\text{-}BW_{11}O_{39})_2]\cdot 23H_2O$ (4). The synthetic procedure of **4** is similar to **1** except that $Ce(NO_3)_3\cdot 6H_2O$ (0.207 g, 0.477 mmol) was replaced by $Sm(NO_3)_3\cdot 6H_2O$ (0.207 g, 0.466 mmol). Pale yellow needle-like crystals of **4** were obtained. Yield: 0.35 g (22.1%) based on $Sm(NO_3)_3\cdot 6H_2O$. Elemental analysis (%) calcd: C, 1.46; H, 1.07; N, 0.85; Na, 1.40; K, 2.38; W, 61.45; Sm, 4.57. Found: C, 1.53; H, 1.12; N, 0.73; Na, 1.60; K, 2.21; W, 61.34; Sm, 4.45. IR (KBr, cm^{-1}): 3394(s), 1621(m), 1477(m), 1412(w), 948(m), 826(s), 702(w), 512(m), 430(w) (Fig. S1†).

$K_4Na_4H_4[Eu_2(gly)_4(\alpha\text{-}BW_{11}O_{39})_2]\cdot 23H_2O$ (5). The synthetic procedure of **5** is similar to **1** except that $Ce(NO_3)_3\cdot 6H_2O$ (0.207 g, 0.477 mmol) was replaced by $Eu(NO_3)_3\cdot 6H_2O$ (0.207 g, 0.464 mmol). Colorless needle-like crystals of **5** were obtained. Yield: 0.29 g (18.2%) based on $Eu(NO_3)_3\cdot 6H_2O$. Elemental analysis (%) calcd: C, 1.46; H, 1.07; N, 0.85, Na, 1.40; K, 2.38; W, 61.42; Eu, 4.62. Found: C, 1.42; H, 1.18; N, 0.79; Na, 1.57; K, 2.47; W, 61.28; Eu, 4.50. IR (KBr, cm^{-1}): 3433(s), 1645(m), 1476(m), 1412(w), 946(m), 821(s), 697(w), 519(m), 431(w) (Fig. S1†).

$K_4Na_4H_4[Tm_2(gly)_4(\alpha\text{-}BW_{11}O_{39})_2]\cdot 23H_2O$ (6). The synthetic procedure of **6** is similar to **1** except that $Ce(NO_3)_3\cdot 6H_2O$ (0.207 g, 0.477 mmol) was replaced by $Tm(NO_3)_3\cdot 6H_2O$ (0.207 g, 0.461 mmol). Colorless needle-like crystals of **6** were obtained. Yield: 0.31 g (19.5%) based on $Tm(NO_3)_3\cdot 6H_2O$. Elemental analysis (%) calcd: C, 1.45; H, 1.07; N, 0.85, Na, 1.39; K, 2.36; W, 61.10; Tm, 5.10. Found: C, 1.48; H, 1.13; N, 0.76; Na, 1.50; K, 2.17; W, 61.21; Tm, 4.92. IR (KBr, cm^{-1}): 3442(s), 1645(m), 1477(m), 1413(w), 947(m), 826(s), 700(w), 519(m), 430(w) (Fig. S1†).

X-ray crystallography

Single-crystal X-ray diffraction data of **1–6** were collected on a Bruker APEX-II CCD detector at 296(2) K with graphite monochromated Mo Kα radiation (λ = 0.71073 Å). Their structures were determined by direct methods and refined on F^2 by the full-matrix least-squares method using the SHELXTL-97 program package.[11] The remaining atoms were found from successive full-matrix least-squares refinements on F^2 and Fourier syntheses. Lorentz polarization and SADABS corrections were applied. All hydrogen atoms attached to carbon and nitrogen atoms were geometrically placed and refined isotropically as a riding model using the default SHELXTL parameters. No hydrogen atoms associated with water molecules were located from the difference Fourier map. All non-hydrogen atoms were refined anisotropically. The structural refinement details of **1–6** are shown in ESI.† The X-ray diffraction crystallographic data and structure refinements for **1–6** are demonstrated in Table 1. Crystallographic data for **1–6** reported in this paper have been deposited in the Cambridge Crystallographic Data Centre with CCDC 1495658–1495663 for **1–6**.

Table 1 X-ray diffraction crystallographic data and structure refinements for **1–6**

	1	**2**	**3**	**4**	**5**	**6**
Empirical formula	$C_8H_{70}B_2K_4N_4Na_4Ce_2O_{109}W_{22}$	$C_8H_{70}B_2K_4N_4Na_4Pr_2O_{109}W_{22}$	$C_8H_{70}B_2K_4N_4Na_4Nd_2O_{109}W_{22}$	$C_8H_{70}B_2K_4N_4Na_4Sm_2O_{109}W_{22}$	$C_8H_{70}B_2K_4N_4Na_4Eu_2O_{109}W_{22}$	$C_8H_{70}B_2K_4N_4Na_4Tm_2O_{109}W_{22}$
Formula weight	6561.60	6563.18	6569.84	6582.06	6585.28	6619.22
Crystal system	Monoclinic	Monoclinic	Monoclinic	Monoclinic	Monoclinic	Monoclinic
Space group	$P2(1)/c$	$P2(1)/c$	$P2(1)/c$	$P2(1)/c$	$P2(1)/c$	$P2(1)/c$
a, Å	11.783(2)	11.7518(9)	11.7456(8)	11.7598(7)	11.7069(7)	11.6408(10)
b, Å	21.459(4)	21.4795(16)	21.6247(15)	21.7014(14)	21.6010(13)	21.7217(18)
c, Å	21.350(4)	21.3507(17)	21.5977(15)	21.7560(14)	21.3932(14)	21.4679(19)
α, °	90	90	90	90	90	90
β, °	91.787(3)	91.9080(10)	92.4380(10)	92.4250(10)	92.3710(10)	92.451(2)
γ, °	90	90	90	90	90	90
V, Å^{-3}	5395.9(17)	5386.4(7)	5480.7(7)	5547.2(6)	5405.3(6)	5423.4(8)
Z	2	2	2	2	2	2
μ, mm^{-1}	24.457	24.559	24.195	24.028	24.733	25.130
F(000)	5784	5788	5792	5800	5804	5828
T, K	296(2)	296(2)	296(2)	296(2)	296(2)	296(2)
Limiting indices	$-13 \le h \le 13$ $-19 \le k \le 25$ $-25 \le l \le 24$	$-13 \le h \le 13$ $-25 \le k \le 17$ $-25 \le l \le 24$	$-13 \le h \le 13$ $-25 \le k \le 25$ $-21 \le l \le 25$	$-13 \le h \le 13$ $-22 \le k \le 25$ $-24 \le l \le 25$	$-13 \le h \le 13$ $-25 \le k \le 20$ $-25 \le l \le 25$	$-13 \le h \le 13$ $-23 \le k \le 25$ $-25 \le l \le 25$
No. of reflections collected	26 214	27 048	27 696	27 769	27 009	27 540
No. of independent reflections	9217	9363	9600	9609	9396	9511
R_{int}	0.0885	0.0636	0.0508	0.0758	0.0498	0.0669
Data/restrains/parameters	9217/180/674	9363/42/680	9600/84/697	9609/66/692	9396 /24/681	9511/31/682
GOF on F^2	1.020	1.038	1.024	1.009	1.010	1.026
Final R indices [$I > 2\sigma(I)$]	$R_1 = 0.0579$ $wR_2 = 0.1310$	$R_1 = 0.0405$ $wR_2 = 0.0724$	$R_1 = 0.0334$ $wR_2 = 0.0791$	$R_1 = 0.0429$ $wR_2 = 0.0654$	$R_1 = 0.0352$ $wR_2 = 0.0811$	$R_1 = 0.0435$ $wR_2 = 0.0856$
R indices (all data)	$R_1 = 0.0886$ $wR_2 = 0.1417$	$R_1 = 0.0674$ $wR_2 = 0.0780$	$R_1 = 0.0439$ $wR_2 = 0.0827$	$R_1 = 0.0779$ $wR_2 = 0.0717$	$R_1 = 0.0472$ $wR_2 = 0.0849$	$R_1 = 0.0731$ $wR_2 = 0.0932$
Largest diff. peak and hole, e Å^{-3}	4.140, −3.155	2.146, −1.681	2.132, −1.838	3.961, −2.173	2.145, −1.761	2.227, −1.606

Results and discussion

Syntheses

LSPs have witnessed tremendous development in the past several decades.[5,6] However, it is still in its infancy in exploiting the realm of LSBs. In this paper, the monovacant precursor $K_8[\alpha\text{-}BW_{11}O_{39}H]\cdot 13H_2O$ was selected as the original material to react with Ln^{3+} cations in the presence of gly ligands in the aqueous solution and a series of organic–inorganic hybrid LSBs **1–6** were successfully obtained. On the basis of a survey of the previously reported literature, it can be easily found that rare examples of LSPs functionalized by amino acid ligands (Table 2) are reported and are mainly confined to arsenotungstates and phosphotungstates although many inorganic–organic hybrid LSPs involving carboxylic acid ligands have been covered. By a close observation of the synthetic methods, preliminary information on the reaction system was gained that an acidic reaction medium can contribute to the aggregation of Ln^{3+} cations, amino acid ligands and POM fragments to produce alluring and complicated architectures. Recently, our group have conducted some research studies on the reaction of POMs with TM and/or Ln^{3+} cations in the presence of amino acids and some progress has been achieved, such as the 1-D polymolybdates with copper-arg linkers $[Cu(arg)_2]_2[(CuO_6)Mo_6O_{18}(As_3O_3)_2]\cdot 4H_2O$ and $[Cu(arg)_2]_3[TeMo_6O_{24}]\cdot 8H_2O$ (arg = L-arginine),[12] and the dimeric thr-decorated heterometallic species $[Ln(H_2O)_8]_2[Fe_4(H_2O)_8(thr)_2][B\text{-}\beta\text{-}XW_9O_{33}]_2\cdot nH_2O$ (X = Sb^{III}, As^{III}).[13] Enlightened by the previous achievements, we tried to introduce the gly ligand into the Ln/BTs system and finally separated the first type of dimeric LSBs bridged by four gly connectors $K_4Na_4H_4[Ln_2(gly)_4(\alpha\text{-}BW_{11}O_{39})_2]\cdot 23H_2O$ [Ln = Ce^{3+} (**1**), Pr^{3+} (**2**), Nd^{3+} (**3**), Sm^{3+} (**4**), Eu^{3+} (**5**), Tm^{3+} (**6**)] by means of the aqueous solution method. It is worth mentioning that, in the case of our synthetic approach, the reaction reagent and the pH value play an imperative role in the formation of the desired products. On the one hand, the used amount of $K_8[\alpha\text{-}BW_{11}O_{39}H]\cdot 13H_2O$ precursor from 2.5 g to 3.0 g is advantageous for improving the yield of the desired compounds. On the other hand, the pH value of 2.4–3.5 is helpful for the generation of target compounds as under this circumstance an acidic reaction environment is essential to avoid the hydrolysis of Ln^{3+} ions and favors the incorporation of gly molecules. Furthermore, the inclusion of gly molecules not only is anticipated to reduce the possibilities of forming precipitations between Ln^{3+} ions and $[\alpha\text{-}BW_{11}O_{39}]^{9-}$ fragments, but also can stabilize the final structures.

Structural description

Bond valence sum (BVS) calculations of **1–6** show that the oxidation states of all W, Ln, and B elements are +6, +3, and +3, respectively (Table S1†). The phase purity of **1–6** was confirmed by the good consistency of the experimental PXRD patterns of the bulk with the simulated PXRD patterns of the single-crystal structural analyses (Fig. S2†).

1–6 are isostructural and belong to the monoclinic space group $P2(1)/c$; all of them possess a particular dimeric structure established by two mono-Ln substituted Keggin $[Ln(\alpha\text{-}BW_{11}O_{39})]^{6-}$ BT subunits bridged by four gly bridges. As far as we know, they stand for the first inorganic–organic hybrid LSBs functionalized by amino acid ligands. Therefore, only **1** is taken as an example to be discussed. The molecular structure of **1** consists of an inorganic–organic hybrid dumbbell-shaped $[Ce_2(gly)_4(BW_{11}O_{39})_2]^{12-}$ polyoxoanion (Fig. 1a), four K^+ ions, four Na^+ ions, four H^+ ions and twenty-three lattice water molecules. It is noteworthy that the centric dumbbell-shaped $[Ce_2(gly)_4(\alpha\text{-}BW_{11}O_{39})_2]^{12-}$ polyoxoanion can be described as the combination of two identical symmetrically related $[Ce(\alpha\text{-}BW_{11}O_{39})]^{6-}$ fragments (Fig. 1b) *via* four gly linkages (Fig. 1c). Two mono-Ln substituted Keggin $[Ce(\alpha\text{-}BW_{11}O_{39})]^{6-}$ symmetrically related fragments display the head-to-head fashion. In the $[\alpha\text{-}BW_{11}O_{39}]^{9-}$ fragment, the central B atom is surrounded by three μ_4-O atoms from three vertex-sharing $\{W_3O_{13}\}$ triads and one μ_3-O atom from an edging-sharing $\{W_2O_{10}\}$ dimer with B–O distances of 1.50(2)–1.53(2) Å and O–B–O bond angles of 104.4(14)–113.6(15)°, leading to a distorted tetrahedral geometry. In **1**, there is one crystallographically unique Ce^{3+} cation that binds to four terminal O atoms (O18, O21, O30, O38) from one $[\alpha\text{-}BW_{11}O_{39}]^{9-}$ subunit [Ce–O: 2.481(13)–2.523(14) Å] and five carboxyl O atoms (O40A, O41, O42, O42A, O43A) [Ce–O: 2.482(14)–2.774(14) Å] from four gly ligands, achieving a nona-coordinate severely distorted monocapped square antiprismatic geometry (Fig. 1d), in which two bottom planes are respectively occupied by O18, O21, O30, O38 groups and O40A, O41, O42, O43A groups while the cap

Table 2 Summary of LSPs functionalized by amino acid molecules

Year	Phases	Major reactants	pH	Synthetic methods
2007	$[Ce_4As_4W_{44}O_{151}(ala)_4(OH)_2(H_2O)_{10}]^{12-}$ [6a]	$K_9Na_7[\{Ce_2O(H_2O)_5\}\{WO(H_2O)\}\{AsW_9O_{33}\}_2]_2\cdot\sim 19.5H_2O$/ala	2.0	Aqueous method
2010	$[Dy_4As_2W_{22}O_{76}(H_2O)_{19}(C_2H_5NO_2)_2]^{2-}$ [6c]	$Dy(NO_3)_3\cdot H_2O$/gly/$K_{14}[As_2W_{19}O_{67}(H_2O)]$	1.55	Aqueous method
2011	$[Ln_4As_5W_{40}O_{144}(H_2O)_{10}(gly)_2]^{21-}$ (Ln = Gd^{3+}, Tb^{3+}, Dy^{3+}, Ho^{3+}, Y^{3+}) [6e]	$K_{14}[As_2W_{19}O_{67}(H_2O)]$/$Ln(NO_3)_3\cdot 6H_2O$/gly/DABCO	5.7	Aqueous method
2011	$K_{1.3}Na_{3.2}H_{6.5}[L\text{-}Pr(PW_{11}O_{39})_2]\cdot 8.3$L-proline$\cdot 21.5H_2O$ [6f] $K_{1.3}Na_{3.2}H_{6.5}[D\text{-}Pr(PW_{11}O_{39})_2]\cdot 8.3$D-proline$\cdot 17H_2O$ $K_{1.3}Na_{3.2}H_{6.5}[L\text{-}Er(PW_{11}O_{39})_2]\cdot 8.3$L-proline$\cdot 22.5H_2O$	$Na_9[A\text{-}\alpha\text{-}PW_9O_{34}]\cdot 16H_2O$/$Ln(NO_3)_3\cdot 6H_2O$/L- or D-proline	1.5	Aqueous method
2013	$[Ln_6(H_2O)_x\{As_4W_{44}(OH)_2(proline)_2O_{151}\}]^{10-}$ (Ln = Tb^{3+}, Dy^{3+}, Nd^{3+}) [6b]	$K_{14}[As_2W_{19}O_{67}(H_2O)]$/$Ln(NO_3)_3\cdot 6H_2O$/L-proline	1.5	Aqueous method
2014	$[As^{III}_4(Y^{III}W^{VI}_3)W^{VI}_{44}Y^{III}_4O_{159}(gly)_8(H_2O)_{14}]^{9-}$ [6d]	$K_{14}[As_2W_{19}O_{67}(H_2O)]$/gly(aq)/$Y(NO_3)_3\cdot 6H_2O$/*p*-MeBzNH$_2$	2.0–2.2	Aqueous method
2015	$KNa_3[HPro]_7[Sm(\alpha\text{-}PW_{11}O_{39})_2]\cdot$Pro$\cdot 18H_2O$ [6g]	$Na_9[A\text{-}\alpha\text{-}PW_9O_{34}]\cdot 7H_2O$/D-proline/$SmCl_3$	1.5	Aqueous method

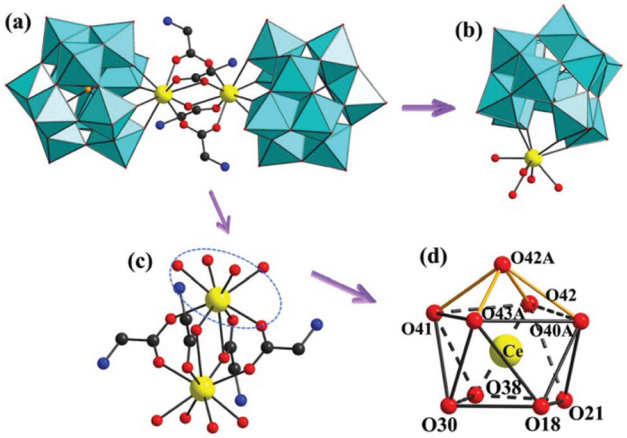

Fig. 1 (a) View of the molecular structure of **1** with the selected labeling scheme. (b) Incorporation of the Ce^{3+} ion into the monolacunary Keggin $[\alpha\text{-}BW_{11}O_{39}]^{9-}$ fragment. (c) The connection between two Ce^{3+} ions and gly ligands in **1**. (d) The coordination sphere of the Ce^{3+} ion in **1**. The atoms with the suffix A are generated by the symmetry operation where A: $1-x$, $1-y$, $1-z$. C: gray-80%, N: blue, O: red, Ce: yellow, B: light orange, $\{WO_6\}$: turquoise.

position is occupied by O42A. The Ce–O bond lengths of 2.481(13)–2.774(14) Å and the O–Ce–O bond angles of 48.8(4)–144.4(5)° are basically within the normal range for a nona-coordinate Ce^{3+} system.[14] There are two crystallographically independent gly molecules, which adopt the didentate coordination fashion and coordinate to two Ce^{3+} cations through carboxylic O atoms with the Ce···Ce distance of 4.124(16) Å (Fig. 2a). It is very fascinating that their binding modes are somewhat different although two gly ligands utilize the didentate coordination fashion, in which both carboxylic O atoms (O40, O41) from the first-type gly ligand display the same μ_2-O pattern, while two carboxylic O atoms (O42, O43) from the second-type gly ligand show the μ_2-O and μ_3-O patterns (Fig. 2b–d). More interestingly, two planes respectively defined by four carboxylic O atoms in each of the two types of gly ligands are almost perpendicular to each other with the dihedral angle of 85.047(7)° (Fig. 2e) and this distribution mode is beneficial to enhance the structural stability of **1**. As far as we are aware, this distribution mode was first encountered among LSPs functionalized by amino acid ligands, delegating a rare example of amino acid inclusion within a POT polyoxoanion in contrast to those containing coordination of gly, ala, or pro ligands *via* carboxylic O atoms in a μ_2-O bridging binding mode to Ln^{3+} cations or W metal centers, or even both of them.[36–40]

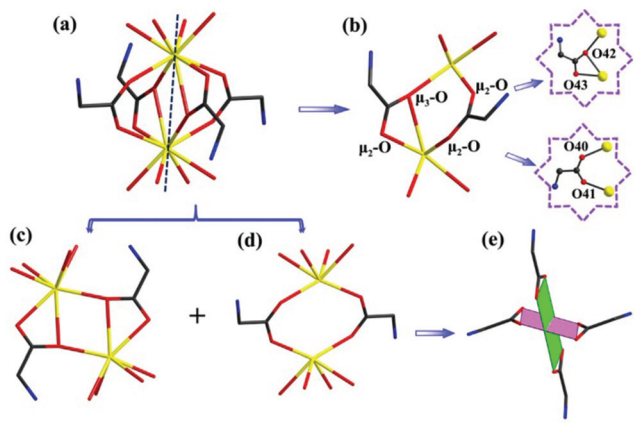

Fig. 2 (a) The $\{Ce_2(gly)_4\}$ cluster in **1**. (b) The μ_2-O and μ_3-O atoms in the $\{Ce_2(gly)_4\}$ cluster. (c) and (d) The connection modes of gly ligands with the Ce^{3+} cations. (e) Two almost perpendicular planes respectively defined by four carboxylic O atoms in each of the two types of gly ligands showing the dihedral angle of 85.0°.

Notably, some inorganic–organic hybrid dimeric LSPs derived from the fusion of two lacunary Keggin-type POT fragments have been addressed (Fig. 3), in which the coordination water molecules grafting to the Ln^{3+} cations can be partially or totally substituted by organic ingredients. One common structure type is that two Ln-substituted POT fragments are connected by organic linkages, giving rise to sandwich-type dimeric LSPs such as the mono-carboxylate bridging complexes $[\{Ln(\alpha\text{-}XW_{11}O_{39})(H_2O)\}_2(\mu\text{-}CH_3COO)_2]^{10/12-}$ (X = P^V, Si^{IV}) (Fig. 3a),[5d–h] di-carboxylate bridging species $\{[(\alpha\text{-}PW_{11}O_{39})Ln(H_2O)]_2(C_2O_4)\}^{10-}$ (Fig. 3b) and $[Ln_2(C_4H_4O_6)(C_4H_2O_6)(AsW_9O_{33})]_2^{18-}$ (Fig. 3c),[5m,r] in which organic components not only participate in the substitution reaction of water ligands but also play an important bridging role in the assembly of dimeric polyoxoanions. The other structure type is related to those dimers decorated by organic ligands such as the W-linked complex $[Tb_2(pic)(H_2O)_2(B\text{-}\beta\text{-}AsW_8O_{30})_2(WO_2(pic))_3]^{10-}$ (Fig. 3d),[5l] the chiral tartrate-based POT $[Ce(H_2O)(CH_3CH_2OH)(L/D\text{-}tartH_3)(Si_2W_{19}O_{66})]^{8-}$ (Fig. 3e),[5s] and the gly-encapsulated polyoxoanion $[Dy_4As_2W_{22}O_{76}(H_2O)_{19}(C_2H_5NO_2)_2]^{2-}$ (Fig. 3f).[6c] Furthermore, water ligands replaced by organic solvent molecules were also observed in $[\{Ln(H_2O)_2(acetone)\}_2(\gamma\text{-}SiW_{10}O_{36})_2]^{10-}$ (Ln = Y^{3+}, Nd^{3+}, Eu^{3+}, Gd^{3+}, Tb^{3+}, Dy^{3+}) (Fig. 3g).[15] In contrast, the feature that four gly molecules coordinate to a Ce^{3+} ion incorporated in the lacunary pocket of the $[\alpha\text{-}BW_{11}O_{39}]^{9-}$ skeleton in **1** makes **1** outstanding among the previously reported dimeric LSPs, and thus **1** represents the first inorganic–organic hybrid gly-functionalized LSB.

Additionally, free $[Ce_2(gly)_4(\alpha\text{-}BW_{11}O_{39})_2]^{12-}$ units are regularly distributed in the arrangement mode of –ABA– (Fig. 4a). A closer examination reveals that neighboring

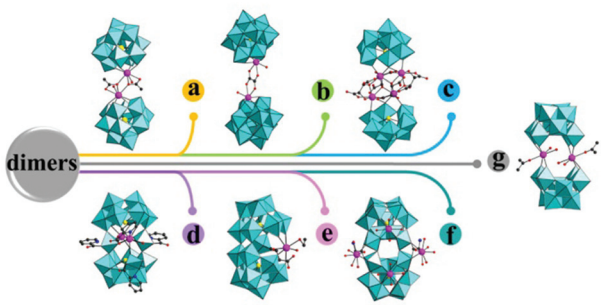

Fig. 3 Some representative inorganic–organic hybrid dimeric LSPs.

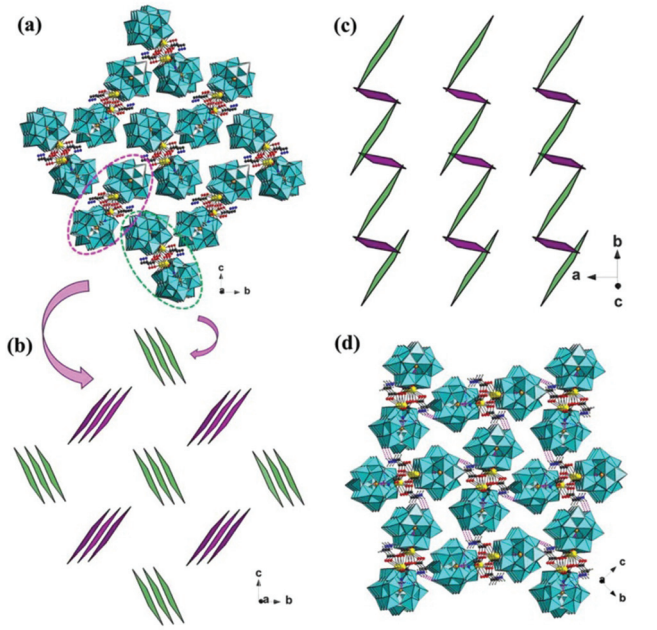

Fig. 4 (a) The 3-D packing of discrete $[Ce_2(gly)_4(\alpha\text{-}BW_{11}O_{39})_2]^{12-}$ units. (b) and (c) The simplified 3-D packing modes in two different directions. (d) The 3-D supramolecular architecture of **1**. Pink bonds highlight the hydrogen-bonding interactions.

$[Ce_2(gly)_4(\alpha\text{-}BW_{11}O_{39})_2]^{12-}$ units are oppositely aligned in a staggered fashion (Fig. 4b and c), which could effectively reduce the steric hindrance and favors the closest packing of $[Ce_2(gly)_4(\alpha\text{-}BW_{11}O_{39})_2]^{12-}$ units. It is worth noting that the incorporation of Ln^{3+} cations into POMs is an important topic in the field of supramolecular chemistry, in which the building blocks formed by Ln^{3+} cations and POMs can be interconnected through hydrogen bonds or van der Waals interactions to generate 3-D supramolecular frameworks and these POM-based supramolecular complexes are promising candidates in the domain of chemicobiology, material chemistry, *etc*. From the view of supramolecular chemistry, 3-D supramolecular architecture also exists in **1** taking into consideration the H-bonding interactions between the N atoms of gly ligands and the surface O atoms of the BT units and water molecules (Fig. 4d and S3†). For each gly molecule, only one N atom participates in the formation of N–H···O interactions as O atoms are totally involved in the coordination with Ln^{3+} cations. Consequently, the combined interactions between the proton donors served by gly ligands and the proton acceptors coming from the surface O atoms of the BT units as well as water molecules lead to the infinitely long 3-D supramolecular structure with the N–H···O distances in the range of 2.83(3)–3.34(3) Å.

Another attractive structural characteristic of **1** is that the dimeric $[Ce_2(gly)_4(\alpha\text{-}BW_{11}O_{39})_2]^{12-}$ units are cemented by bridging K^+ and Na^+ ions propagating the beauteous 3-D architecture (Fig. 5a and S4†). It is exciting to find that two $\{K_2Na_2\}$ clusters like two arms are situated on both sides of the central $\{Ce_2(gly)_4\}$ unit (Fig. 5b and S5†) to "shake hands" with neighboring $\{BW_{11}O_{39}\}$ fragments and accomplish the assembly of

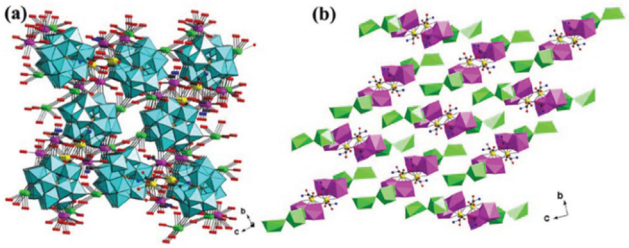

Fig. 5 (a) The 3-D architecture constructed from the K^+ and Na^+ cations in **1**. (b) The regular alignment of the $\{K_4Na_4Ce_2(gly)_4\}$ cluster in the 3-D structure of **1**. $\{KO_8\}$: pink; $\{NaO_6\}$ and $\{NaO_7\}$: bright green.

the 3-D structure. As far as we are aware, alkali metal cations such as K^+ or Na^+ ions originating from starting materials or additional alkali metal salts play an important role in the assembly of the final products in the POT chemistry. Generally speaking, the functionalities of alkali metal cations can be summarized into three aspects except the common role of charge compensation: (i) the regulating effect: in 2006, Gutiérrez-Zorrilla *et al.* discovered that when Na^+, K^+, and Rb^+ acetate buffers are respectively used, three different silicotungstates, $K_8[\{Si_2W_{22}Cu_2O_{78}(H_2O)\}\{Cu_2(ac)_2(phen)_2(H_2O)\}_2]\cdot\sim40H_2O$, $K_4[\{SiW_{11}O_{39}Cu(H_2O)\}\{Cu_2(ac)_2(phen)_2(H_2O)\}]\cdot14H_2O$ and $Cs_7[Cu_2(ac)_2(phen)_2(H_2O)_2][Cu_3(ac)_3(phen)_3(H_2O)_3][Si_2W_{22}Cu_2O_{78}(H_2O)]\cdot\sim18H_2O$ (ac = acetate, phen = 1,10-phenanthroline), were obtained, indicating that the structures of the outcomes highly depend on the size of alkaline cations.[16] Afterwards, Zhao *et al.* further confirmed this viewpoint.[17] (ii) The template effect: in this respect, the K^+ ion is encapsulated in the cavity and plays a key role in the formation and stabilization of the whole structure,[18] such as the unprecedented crown-shaped species $[K\subset K_7Ce_{24}Ge_{12}W_{120}O_{456}(OH)_{12}(H_2O)_{64}]^{52-}$ that can be regarded as the outcome of the K^+-directed self-assembly of twelve $[Ce_2GeW_{10}O_{38}]^{6-}$ units.[18a] (iii) The bridging effect: alkali metal cations usually have a high affinity for the POT anions as well as solvent molecules and are liable to associate with terminal O groups of the polyoxoanions to produce $[M(H_2O)_n]^+$ units, conducive to the construction of polymeric or high-dimensional POTs.[19]

IR spectra

The IR spectra of **1–6** have been recorded in the range of 4000–400 cm^{-1} from solid samples palletized with KBr, which are presented in Fig. S1.† It is obviously seen that all of them have similar four characteristic vibration patterns in the low wavenumber range (ν < 1000 cm^{-1}), corresponding to the analogous basic BT fragments in their skeletons. The four characteristic peaks at 948, 877, 822 and 691 cm^{-1} for **1**, 947, 878, 819 and 691 cm^{-1} for **2**, 946, 874, 819 and 697 cm^{-1} for **3**, 948, 877, 826 and 702 cm^{-1} for **4**, 946, 875, 821 and 697 cm^{-1} for **5**, and 947, 878, 826 and 700 cm^{-1} for **6** are respectively ascribed to the terminal $\nu(W\text{–}O_t)$, $\nu(B\text{–}O)$, corner-sharing $\nu(W\text{–}O_b)$ and edge-sharing $\nu(W\text{–}O_c)$ of the $[\alpha\text{-}BW_{11}O_{39}]^{9-}$

polyoxoanion. Compared to $K_8[\alpha\text{-}BW_{11}O_{39}H]\cdot 13H_2O$ [954, 886, 837 and 745 cm^{-1} for $\nu(W\text{–}O_t)$, $\nu(B\text{–}O)$, $\nu(W\text{–}O_b)$ and $\nu(W\text{–}O_c)$], the shifts of $\nu(W\text{–}O_t)$, $\nu(B\text{–}O)$, $\nu(W\text{–}O_b)$ and $\nu(W\text{–}O_c)$ are related to the implantation of the Ln^{3+} cation to the defect site of the $[\alpha\text{-}BW_{11}O_{39}]^{9-}$ segment, leading to the deformation and distortion of the $[\alpha\text{-}BW_{11}O_{39}]^{9-}$ skeleton. In the high wavenumber region ($\nu > 1000$ cm^{-1}), an intense and broad absorption band at 3394–3442 cm^{-1} as well as a strong absorption band at 1621–1645 cm^{-1} are observed, which are ascribed to the stretching and bending vibration modes of water molecules, respectively. It should be noted that there is some overlap between the $\nu(C{=}O)$ absorption band of gly ligands and the intense bending vibration band of water molecules. In the IR spectrum of the free gly ligand, the asymmetric and symmetric vibrations of the carboxylate group are seen at 1621 cm^{-1} and 1413 cm^{-1}. Compared with the free gly ligand, the appearance of weak peaks derived from asymmetric and symmetric vibrations of the carboxylate group of the gly ligand in the IR spectra of **1–6** is indicative of the presence of gly components in **1–6**. Specifically, the resonances at 1624–1640 cm^{-1} and 1412–1416 cm^{-1} are discriminably attributed to the asymmetric stretching vibration and symmetric stretching vibration of the carboxylate groups [named $\nu_{as}(COO)$ and $\nu_s(COO)$, respectively], which have some shifts to some extent in contrast to the free gly ligand, suggesting that the gly ligand coordinates to the Ln^{3+} cations. Generally speaking, the difference ($\Delta\nu$) between the $\nu_{as}(COO)$ and $\nu_s(COO)$ is often applied as a criterion to evaluate the coordination mode of the carboxylate group.[5k,20] Herein, the $\Delta\nu$ of 212–224 cm^{-1} in **1–6** demonstrates that the gly ligands in **1–6** employ the bridging coordination mode, which is in good agreement with the results of X-ray single-crystal diffraction. In addition, the peak located at 1339–1343 cm^{-1} is assigned to the $\nu(C\text{–}N)$ vibration, while the Ln–O stretching vibrations of **1–6** are absent in the IR region probably resulting from the prominent ionic interactions between the lacunary POT segments and Ln^{3+} cations.[5d]

Photoluminescence (PL) properties

The PL properties of Ln^{3+} ions have been fascinating researchers for several decades and has evoked great interest in the biomedical analyses, cathode ray tubes, light-emitting diodes, fluorescent tubes and efficient light conversion molecular devices due to their particular luminescence features such as high luminescence quantum yield, narrow bandwidth, long-lived emission and large Stokes shift.[21] As is well known, Eu^{3+} and Tb^{3+} complexes are the most intense emitters that respectively emit red and green light among the Ln series, and are widely used as luminescence materials for easily detected emissions in the visible region, while Nd^{3+}, Er^{3+}, and Yb^{3+} complexes are applied in biological analysis for their almost transparent near-infrared (NIR) emissions in biological issues.[22] These unique functionalities are assigned to the transitions inside the 4f shell of Ln^{3+} ions involved in the shielding of the partially filled 4f orbits by the closed $5s^2$ and $5p^6$ shells, resulting in the characteristic narrow line-like emissions[2,3] and the long lifetimes of the excited states. In this paper, the luminescence properties and lifetime decay behaviors of **3**, **4** and **5** in the solid state were investigated at ambient temperature.

When **3** is excited at 584 nm, its NIR PL emission spectrum (Fig. 6a) displays three characteristic emission bands, which are assigned to $^4F_{3/2} \rightarrow {}^4I_{9/2}$ (870 and 892 nm), $^4F_{3/2} \rightarrow {}^4I_{11/2}$ (1059 nm) and $^4F_{3/2} \rightarrow {}^4I_{13/2}$ (1334 nm) transitions of Nd^{3+} ions, respectively.[24] In terms of Nd^{3+} excitation, some transitions to different states are not resolved and the excitation bands are relatively broad on account of the multiplicity of excited 4f states in the visible region. Hence, several bands were apperceived in the excitation spectrum monitored at the $^4F_{3/2} \rightarrow {}^4I_{11/2}$ transition at 1059 nm for **3**, corresponding to the Nd^{3+} f–f transitions located at 515 nm ($^4I_{9/2} \rightarrow {}^2K_{13/2}$), 526 nm ($^4I_{9/2} \rightarrow {}^4G_{7/2}/{}^4G_{9/2}$), 584 nm ($^4I_{9/2} \rightarrow {}^4G_{5/2}/{}^2G_{7/2}$), and 628 nm ($^4I_{9/2} \rightarrow {}^2H_{11/2}$) (Fig. 6a). In order to determine the lifetime, the luminescence decay curve of **3** (Fig. 6c) by monitoring at the strongest emission of $^4F_{3/2} \rightarrow {}^4I_{11/2}$ was carried out, which can be fitted to a double exponential function $I = A_1\exp(-t/\tau_1) + A_2\exp(-t/\tau_2)$ (where τ_1 and τ_2 are the fast and slow components of the luminescence lifetimes; A_1 and A_2 are the pre-exponential factors), affording the luminescence lifetimes τ_1 and τ_2 as 0.96 μs (17.91%) and 9.99 μs (82.09%), and the agreement factors (χ^2) of 1.296, respectively. The average lifetime (τ) of **3** is 8.38 μs based on the formula $\tau = [A_1{\tau_1}^2 + A_2{\tau_2}^2]/[A_1\tau_1 + A_2\tau_2]$ (Table S2†).[25] Theoretically, the lifetime decay of **3** should abide by a single exponential function since there is only one crystallographically unique Nd^{3+} ion in the structure. To gain insight into the origin of two lifetimes of **3**, the luminescence emission of the precursor $K_8[\alpha\text{-}BW_{11}O_{39}H]\cdot 13H_2O$ was performed under the similar conditions to **3**. Unfortunately, $K_8[\alpha\text{-}BW_{11}O_{39}H]\cdot 13H_2O$ does not exhibit any luminescence emission in the NIR region (Fig. S6†). As a consequence, it can be inferred that the di-exponential decay behavior of **3** may be attributed to the interactions between Nd^{3+} centers (the $Nd^{3+}\cdots Nd^{3+}$ distance is 4.1152(2) Å, which comes from the result of X-ray single-crystal diffraction).

The solid-state PL emission spectrum of **4** (Fig. 6d) under excitation at 403 nm was measured at room temperature, giving birth to the pink emission of Sm^{3+} ion originating from the $^4G_{5/2}$ level appearing at 561, 597, 605, 648, and 705 nm, respectively. The strongest emission peaks located at 597 nm with a splitting peak around 605 nm are derived from the $^4G_{5/2} \rightarrow {}^6H_{7/2}$ transition of Sm^{3+} while the peaks centered at 561, 648 and 705 nm are severally attributed to $^4G_{5/2} \rightarrow {}^6H_{5/2}$, $^4G_{5/2} \rightarrow {}^6H_{9/2}$ and $^4G_{5/2} \rightarrow {}^6H_{11/2}$, respectively.[26] The excitation spectrum of **4** (Fig. 6e) detected at the Sm^{3+} $^4G_{5/2} \rightarrow {}^6H_{7/2}$ transition (597 nm) is dominated by the $^6H_{5/2} \rightarrow {}^4F_{7/2}$ transition at 403 nm, whereas the observable weaker peaks can be assigned to the transitions from the $^6H_{5/2}$ ground state to the $^4H_{9/2}$ at 346 nm, $^4D_{5/2}$ at 363 nm, $^6P_{7/2}$ at 376 nm, $^6G_{11/2}$ at 391 nm, $^6P_{5/2}$ at 417 nm and $^4G_{9/2}$ at 441 nm, respectively.[26] The lifetime decay curve for $^4G_{5/2}$ level of **4** (Fig. 6f) under excitation at 403 nm and emission at 597 nm can be fitted to a double exponential function generating the lifetime values τ_1 and τ_2 of 3.95 μs (50.12%) and 9.00 μs (49.88%) with the average lifetime

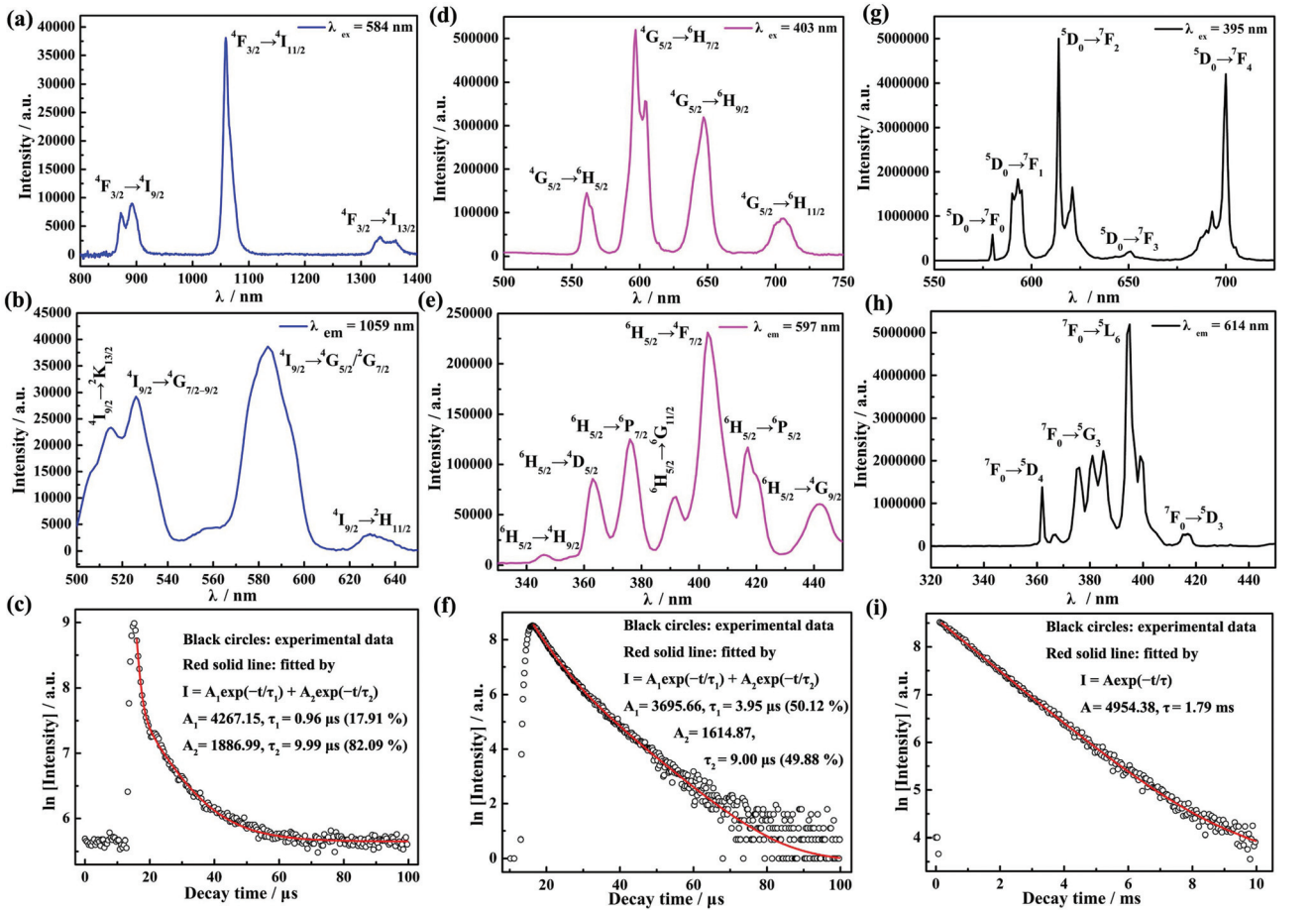

Fig. 6 (a) The solid-state emission spectrum of **3** (λ_{ex} = 584 nm) at room temperature. (b) The solid-state excitation spectrum of **3** (λ_{em} = 1059 nm) at room temperature. (c) The luminescence decay curve of **3** taken by monitoring the emission at 1059 nm with τ_1 and τ_2 of 0.96 μs (17.91%) and 9.99 μs (82.09%). (d) The solid-state emission spectrum of **4** (λ_{ex} = 403 nm) at room temperature. (e) The solid-state excitation spectrum of **4** (λ_{em} = 597 nm) at room temperature. (f) The luminescence decay curve of **4** taken by monitoring the emission at 597 nm with τ_1 and τ_2 of 3.95 μs (17.91%) and 9.00 μs (82.09%). (g) The solid-state emission spectrum of **5** (λ_{ex} = 395 nm) at room temperature. (h) The solid-state excitation spectrum of **5** (λ_{em} = 614 nm) at room temperature. (i) The luminescence decay curve of **5** taken by monitoring the emission at 614 nm with τ of 1.97 ms.

of 6.47 μs and the agreement factor (χ^2) of 1.073. Under similar conditions, the luminescence emission spectrum and the lifetime decay curve of the precursor $K_8[\alpha\text{-}BW_{11}O_{39}H]\cdot 13H_2O$ were examined under emission at 597 nm and excitation at 403 nm. The emission spectrum of $K_8[\alpha\text{-}BW_{11}O_{39}H]\cdot 13H_2O$ reveals a broad band at around 700 nm (Fig. S7†), the intensity of which is relatively weak so that it was overlapped by the typical peak $^4G_{5/2} \rightarrow {}^6H_{11/2}$ of **4** at 705 nm, suggesting that the energy transfer from the $[\alpha\text{-}BW_{11}O_{39}]^{9-}$ fragments to Sm^{3+} centers may happen. This result is further confirmed by the bi-exponential decay curve of $K_8[\alpha\text{-}BW_{11}O_{39}H]\cdot 13H_2O$ with τ_1 = 1.68 μs (42.21%) and τ_2 = 9.31 μs (57.79%) (Fig. S8†). The average lifetime is calculated to be 6.09 μs, approximately to that of **4** (Fig. 7a), thus it can be reasonably assessed that the $[\alpha\text{-}BW_{11}O_{39}]^{9-}$ fragments make some of the contribution to the PL behavior of **4** by the energy transfer of the O → W transitions to Sm^{3+} centers during the emission process of **4**. As an important parameter to characterize the efficiency of the emission process, the luminescence quantum yields (Φ) of **4** and $K_8[\alpha\text{-}BW_{11}O_{39}H]\cdot 13H_2O$ were determined using an integrating sphere at ambient temperature under excitation at 403 nm, and the emission quantum yields are found to be 7.45% (Fig. S9†) and 5.98% (Fig. S10†), respectively. The relatively similar Φ values further confirm the energy transfer from $K_8[\alpha\text{-}BW_{11}O_{39}H]\cdot 13H_2O$ to **4** in the emission procedure.

The emission spectrum of **5** (Fig. 6g) was recorded under a maximum excitation at 395 nm; it exhibits the characteristic luminescence bands of Eu^{3+} ions centered at 580, 593, 614, 651 and 700 nm, attributed to the $^5D_0 \rightarrow {}^7F_J$ (J = 0–4) transitions, respectively. The $^5D_0 \rightarrow {}^7F_{1,3}$ transitions are magnetic-dipolar transitions that are insensitive to their local environments whereas the $^5D_0 \rightarrow {}^7F_{0,2,4}$ transitions are electro-dipolar transitions that are fairly hypersensitive to their local environments.[27] As we know, the $^5D_0 \rightarrow {}^7F_0$ emission is severely forbidden in a symmetric field, but the appearance of this symmetric forbidden transition at 580 nm in **5** suggests that the Eu^{3+} ions are situated in the lower symmetric ligand field.

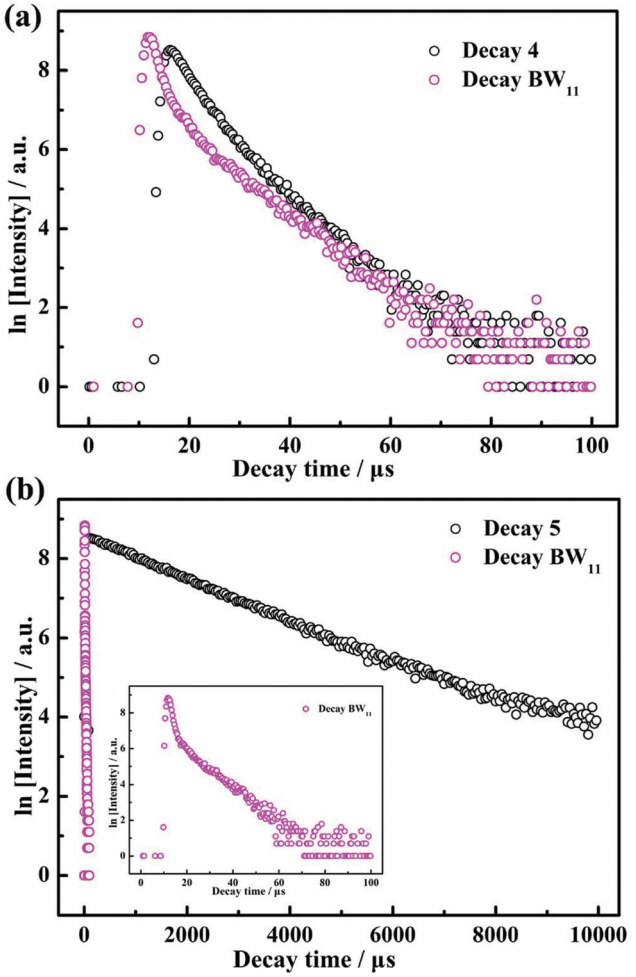

Fig. 7 (a) The luminescence decay curves of **4** and $K_8[\alpha\text{-}BW_{11}O_{39}H]\cdot 13H_2O$ (BW_{11}) taken by monitoring the emission at 597 nm. (b) The luminescence decay curves of **5** and BW_{11} taken by monitoring the emission at 614 nm. Insert: an enlarged view of the decay curve of BW_{11}.

Moreover, the $^5D_0 \rightarrow {}^7F_0$ transition just exhibits a single peak, from which we can also draw a conclusion on the low symmetry site of the Eu^{3+} ion in good agreement with the monocapped square antiprismatic geometry. The medium–strong emission at 593 nm is ascribed to the magnetic-dipole transition from $^5D_0 \rightarrow {}^7F_1$ and its emission intensity barely varies with the strength of the ligand field acting on the Eu^{3+} ion. In contrast, the most intense emission at 614 nm assigned to the electro-dipolar transition from the $^5D_0 \rightarrow {}^7F_2$ transition is highly sensitive to the coordination environment of the Eu^{3+} ion and implies a red emission light. Generally speaking, the Eu^{3+} ion can be regarded as an excellent structure probe for the investigation of the local environment in a host matrix on the basis of Judd–Ofelt theory.[28] If the Eu^{3+} ion is located in a centrosymmetric environment, the $^5D_0 \rightarrow {}^7F_1$ transition should be dominant and in a noncentrosymmetric situation, the $^5D_0 \rightarrow {}^7F_2$ transition would be the preponderant one.[29] As depicted in Fig. 6g, the intensities of $^5D_0 \rightarrow {}^7F_{2,4}$ transitions are much stronger than those of $^5D_0 \rightarrow {}^7F_{1,3}$, testifying that the Eu^{3+} ion does not reside in the inversion symmetric environment. Besides, the intensity of the $^5D_0 \rightarrow {}^7F_2$ transition increases as the site symmetry of the Eu^{3+} center decreases. Thus, the intensity ratio of $I(^5D_0 \rightarrow {}^7F_2)/I(^5D_0 \rightarrow {}^7F_1)$ is usually used as a criterion of the change in the nature of Eu^{3+} local surroundings as well as the site symmetry of the Eu^{3+} ion.[30] In this work, the intensity ratio is *ca.* 2.7, showing that the site environment of the Eu^{3+} ion is asymmetric, consistent with the results of the single-crystal X-ray analysis. These values are lower than those observed for the Eu^{3+} ions in $[Eu(H_2O)_8]_2[Fe_4(H_2O)_8(thr)_2][B\text{-}\beta\text{-}SbW_9O_{33}]_2\cdot 22H_2O$ (4.7),[13a] $[Eu(pqc)(Hpqc)(NO_3)_2]_n$ (5.5)[31] and $Cs_3K_4[(Ge_2W_{18}Nb_6O_{78})Eu(H_2O)_4]\cdot 23H_2O$ (7.3).[32] A greater intensity ratio may be related to a more distorted local cation environment. The excitation spectrum collected by monitoring the emission at 614 nm is presented in Fig. 6h, and the most intense peak is located at 395 nm ($^7F_0 \rightarrow {}^5L_6$) whereas other weak peaks are observed at 362 nm ($^7F_0 \rightarrow {}^5D_4$), 374–385 nm ($^7F_0 \rightarrow {}^5G_3$) and 416 nm ($^7F_0 \rightarrow {}^5D_3$).[26] The luminescence lifetime of **5** was determined and can be fitted to a single exponential function, $I = A\exp(-t/\tau)$, yielding a lifetime τ of 1.79 ms (Fig. 6i). In contrast, the luminescence lifetimes of $[Eu(H_2O)_8]_2[Fe_4(H_2O)_8(thr)_2][B\text{-}\beta\text{-}SbW_9O_{33}]_2\cdot 22H_2O$ (0.097 ms)[13a] in which the Eu^{3+} ion is surrounded by eight water molecules and $Na_{0.5}Cs_{4.5}[Eu(\alpha\text{-}SiW_{11}O_{39})(H_2O)_2]\cdot 23H_2O$ (0.39 ms)[33] in which two coordinate O atoms of the Eu^{3+} ion are derived from two water ligands are evidently shorter than those of **5**, mainly resulting from the enhancement of the radiationless deactivation of the $^5D_0$ state and partial luminescence quench by the coordinated water ligands.[34] It should be noted that the emission characteristics are largely dependent on the environment of a given Ln^{3+} ion, such as the nature of a POM ligand, the symmetry and coordination geometry of the Ln^{3+} centers as well as the number of aqua coligands. On the one hand, the presence of aqua ligands can lead to quenching of the Ln^{3+}emission and shorting of the luminescence lifetimes by coupling with proximal OH oscillators;[19c] thus slightly shorter decay lifetimes of $[Eu(H_2O)_8]_2[Fe_4(H_2O)_8(thr)_2][B\text{-}\beta\text{-}SbW_9O_{33}]_2\cdot 22H_2O$ and $Na_{0.5}Cs_{4.5}[Eu(\alpha\text{-}SiW_{11}O_{39})(H_2O)_2]\cdot 23H_2O$ can be expected. On the other hand, Ln^{3+} cations usually suffer from weak luminescence due to the weak absorption coefficient (<10 mol^{-1} L cm^{-1}) resulting from spin- and parity-forbidden f–f transitions.[35] This drawback can be overcome by the so-called "antenna effect" in which organic ligands containing O or N atoms with suitable chromophores and tailored coordinate sites are utilized as sensitizers and connectors to absorb light and transfer energy from the organic ligands to the Ln^{3+} ions by intramolecular energy transfer.[36] Thus, the longer decay time of **5** is probably because of the chelation of gly ligands with Eu^{3+} cations precluding the coordination of quenching species such as water molecules to Eu^{3+} centers, thereby reducing the nonradiative decay processes. Moreover, the PL emission and lifetime decay curves of $K_8[\alpha\text{-}BW_{11}O_{39}H]\cdot 13H_2O$ were determined under the same conditions. The wide emission band at 576 nm was also unveiled (Fig. S11†), whilst the

lifetime decay curve of $K_8[\alpha\text{-}BW_{11}O_{39}H]\cdot 13H_2O$ follows a bi-exponential decay function with τ_1 and τ_2 of 1.08 μs (44.19%) and 9.36 μs (55.81%) (Fig. S12†) and the average lifetime is calculated to be 5.70 μs. In comparison with the decay lifetime of **5** (1.79 ms), the lifetime contribution of the $[\alpha\text{-}BW_{11}O_{39}]^{9-}$ fragments in **5** can be almost negligible (Fig. 7b). Besides, the solid-state measurements of the luminescence quantum yields of **5** and $K_8[\alpha\text{-}BW_{11}O_{39}H]\cdot 13H_2O$ under the strongest excitation at 395 nm are 38.45% for **5** (Fig. S13†) and 4.41% for $K_8[\alpha\text{-}BW_{11}O_{39}H]\cdot 13H_2O$ (Fig. S14†), which also demonstrates the weak contribution of $K_8[\alpha\text{-}BW_{11}O_{39}H]\cdot 13H_2O$ in the emission of **5**.

The CIE 1931 diagram offers a pervasive method for studying the possible colors by combining three basic colors (red, blue and green) together, and has been widely utilized to quantify the tunability of the emission wavelength and the change of the emission intensity; as a result, good knowledge of the trueness of color is significant in the realm of lighting and display devices.[37] In the CIE chromaticity diagram, the chromaticity coordinates x and y, where, roughly speaking, x represents the red-to-blue ratio and y represents the green-to-blue ratio, are meaningful to determine the exact emission color of the sample when the white light emission is situated at the center position with the standard chromaticity coordinates (x = 0.33333, y = 0.33333). Here, the CIE chromaticity coordinates of **4** (0.59872, 0.40057) and **5** (0.63983, 0.35981) that are converted from their corresponding emission spectra are presented in Fig. S15.†

Magnetic properties

The last few years have witnessed a large renaissance in the study of Ln^{3+} complexes owing to their large inherent anisotropy and unique electronic configuration such as the large number of unpaired 4f electrons. It is generally known that orbitally degenerate ground states of most Ln^{3+} ions, except for the isotropic Gd^{3+} ion with an $^8S_{7/2}$ single-ion ground state, are split by the spin–orbital coupling and crystal field effect.[38] Nevertheless, spin–orbital coupling interactions play a much more important role in the magnetic behaviors of Ln^{3+} cations compared with the small crystal field effect, as the large spin–orbital coupling can partly remove the degeneracy of the ^{2S+1}L group term of the $4f^n$ configuration for a Ln^{3+} cation, generating $^{2S+1}L_J$ spectroscopic levels by the interelectronic repulsion and spin–orbit coupling, and each of these states is further split into Stark sublevels by the crystal field perturbation.[38,39] As a consequence, the orbital contribution of the magnetic moment is more significant for Ln^{3+} cations.[40] Besides, the $^{2S+1}L_J$ free-ground state for almost all the Ln^{3+} cations is perfectly separated from the first excited state in energy so that only the ground state is thermally populated at ambient and low temperature.[40,41] But when it comes to Eu^{3+} and Sm^{3+}, this situation is evidently different. The first excited state may be thermally populated owing to the small energy separation of 400 cm^{-1} for Eu^{3+} and 1000 cm^{-1} for Sm^{3+} ions; thus the possible crystal field effect as well as the thermal population of the higher energy state should be considered with regard to Eu^{3+}- or Sm^{3+}-containing POMs.[39] With the temperature decreasing, the effective magnetic moment of Ln^{3+} cations will alter by thermal depopulation of the Stark sublevels and the temperature dependence leads to the deviation of magnetic susceptibility from the Curie behavior.[42]

Variable-temperature magnetic susceptibility measurements for **1**, **2** and **4** were preliminarily investigated in the temperature range of 1.8–300 K under a field of 1000 Oe. The plots of $\chi_M T$ *vs.* T and χ_M *vs.* T of **1**, **2** and **4** are displayed in Fig. 8. As for **1**, the $\chi_M T$ value at 300 K is 1.613 $emu^3\ K\ mol^{-1}$, close to the theoretical value of 1.607 $emu^3\ K\ mol^{-1}$ for two non-interacting Ce^{3+} ions (S = 1/2, L = 3, g = 6/7)[43] (Fig. 8a). Upon cooling, the $\chi_M T$ value decreases to a minimum of 0.725 $emu^3\ K\ mol^{-1}$ at 1.8 K. This behavior can mainly be due to the

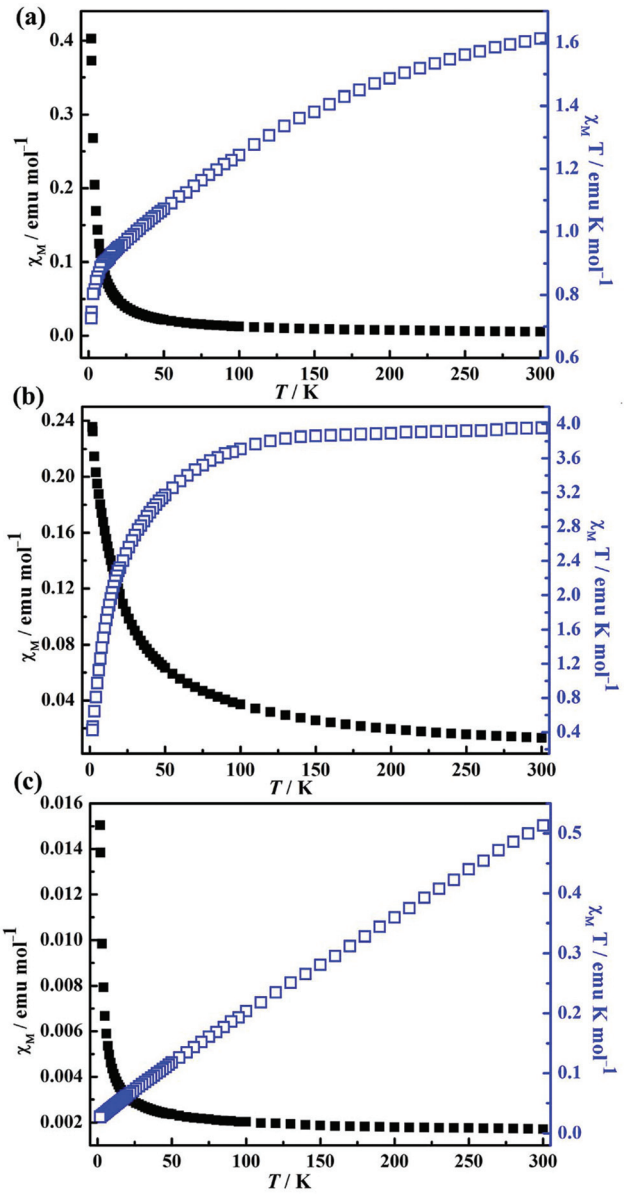

Fig. 8 Temperature dependence of the χ_M and $\chi_M T$ products at 1000 Oe for **1** (a), **2** (b) and **4** (c).

splitting of the 6-fold degenerate $^2F_{5/2}$ ground state affected by the crystal field perturbation and the progressive depopulation of the higher energy state upon cooling.[5d,44] It is well known that all the Stark levels split from the 6-fold degenerate $^2F_{5/2}$ ground state are equally populated at room temperature and with the temperature lowering, the Kramer's doublets of higher energy are depopulated successively, causing the decline of the $\chi_M T$ value with decreasing the temperature.[42]

With respect to **2**, the room-temperature $\chi_M T$ value of 3.955 emu^3 K mol^{-1} is slightly higher than the expected value of 3.20 emu^3 K mol^{-1} for two non-interacting Pr^{3+} ions (S = 1, L = 5, g = 4/5) in the ground state (Fig. 8b). On the whole, the $\chi_M T$ value gradually decreases to reach a value of 0.424 emu^3 K mol^{-1} as the temperature is lowered down to 1.8 K. For all we know, the 9-fold degenerate $^3H_4$ ground state of Pr^{3+} ions could be split into Stark levels by the crystal-field effect. As a result, the declining of $\chi_M T$ values with the decrease of temperature can be ascribed to the progressive population of the higher Stark levels for Pr^{3+} ions.[45]

In the case of **4**, the experimental $\chi_M T$ value at 300 K is 0.513 emu^3 K mol^{-1}, slightly higher than the expected value of 0.178 emu^3 K mol^{-1} for two non-interacting Sm^{3+} ions ($^6H_{5/2}$, J = 5/2, g = 2/7),[46] as illuminated in Fig. 8c. As temperature descends, a linear decrease in $\chi_M T$ value is observed in the experimental data, maybe indicating the occurrence of antiferromagnetic couplings and the depopulation of the Kramer's doublets of the higher energy of the Sm^{3+}. As is known, the $^6H_{5/2}$ ground-state term of the Sm^{3+} ion in the crystal field can be split into six levels (J = 5/2, 7/2, 9/2, 11/2, 13/2, 15/2,) by spin–orbit coupling interactions, and the spin–orbit coupling parameter is 1200 cm^{-1}, therefore the crystal field effect and the possible thermal population of the high energy states should be considered for **4**.[17] The minimum value of 0.027 emu^3 K mol^{-1} at 1.8 K is much smaller than that of two non-interacting Sm^{3+} ions (0.178 emu^3 K mol^{-1}), demonstrating the presence of the comparatively stronger antiferromagnetic exchange interactions within the $\{Sm_2\}$ cluster mediated by the bridging carboxylic oxygen atoms from gly ligands as well as the spin–orbital coupling and the crystal field effect. A similar magnetic phenomenon has been encountered in the Sm^{3+} complex $\{Na[Sm(pydc\text{-}OH)(H_2O)_4]_3\}[SiW_{12}O_{40}]\cdot 15H_2O$.[5t]

Conclusions

In conclusion, a series of novel organic–inorganic hybrid gly-bridging dimeric Keggin-type LSBs **1–6** have been prepared from the BT precursor and Ln^{3+} cations in the presence of gly ligand by using an aqueous solution method; they represent the first LSBs to be functionalized by amino acid ingredients. The PL and lifetime decay behaviors of **3–5** and the magnetic properties of **1**, **2** and **4** have been studied. Furthermore, the thermal decomposition process of **3** has been intensively probed using the TG curves together with the variable-temperature PXRD patterns and variable-temperature IR spectra. This work shows that a great deal of rational structural design in the realm of organic–organic hybrid LSBs is possible. A further study will be carried out utilizing other functionalized amino acid and multi-carboxylic ligands to sensitize the PL emission of Ln^{3+} cations and tune the magnetic interactions of Ln^{3+} cations, as well as exploiting the incorporation of TM cations to ulteriorly open up a new area in heterometallic BT chemistry.

Acknowledgements

This work was supported by the Natural Science Foundation of China (21301049, U1304208, 21571048, and 21671054), the Program for Science & Technology Innovation Talents in Universities of Henan Province (16HASTIT001), the Innovation Scientists and Technicians Troop Construction Projects of Henan Province, the Natural Science Foundation of Henan Province (142300410451), the Postdoctoral Foundation of Henan Province (20140025), the Foundation of State Key Laboratory of Structural Chemistry (20160016), the 2014 Special Foundation for Scientific Research Project of Henan University (XXJC20140001), the 2012 Young Backbone Teachers Foundation from Henan Province (2012GGJS-027) and the 2015, 2016 Students Innovative Pilot Plan of Henan University.

References

1 (*a*) I. V. Kozhevnikov, *Chem. Rev.*, 1998, **98**, 171; (*b*) A. Müller and F. Peters, *Chem. Rev.*, 1998, **98**, 239; (*c*) J. Zhou, J. W. Zhao, Q. Wei, J. Zhang and G. Y. Yang, *J. Am. Chem. Soc.*, 2014, **136**, 5065; (*d*) J. T. Rhule, C. L. Hill and D. A. Judd, *Chem. Rev.*, 1998, **98**, 327; (*e*) E. Coronado and C. J. Gómez-García, *Chem. Rev.*, 1998, **98**, 273; (*f*) S. G. Mitchell, C. Streb, H. N. Miras, T. Boyd, D. L. Long and L. Cronin, *Nat. Chem.*, 2010, **2**, 308; (*g*) Y. F. Wang and I. A. Weinstock, *Chem. Soc. Rev.*, 2012, **41**, 7479; (*h*) C. Fleming, D. L. Long, N. McMillan, J. Johnston, N. Bovet, V. Dhanak, N. Gadegaard, P. Kögerler, L. Cronin and M. Kadodwala, *Nat. Nanotechnol.*, 2008, **3**, 289.

2 (*a*) V. E. Simmons and L. C. W. Baker, *Proc. VII I.C.C.C., Stockholm*, 1962, 195; (*b*) L. C. W. Baker and V. E. Simmons, *Proc. IX I.C.C.C., St. Moritz*, 1966, 421.

3 G. A. Barbieri, *Atti. Accad. Nazi. Lincei*, 1914, **11**, 805.

4 (*a*) R. D. Peacock and T. J. R. Weakley, *J. Chem. Soc. A*, 1971, 1836; (*b*) R. D. Peacock and T. J. R. Weakley, *J. Chem. Soc. A*, 1971, 1937.

5 (*a*) K. Wassermann, M. H. Dickman and M. T. Pope, *Angew. Chem., Int. Ed. Engl.*, 1997, **36**, 1445; (*b*) F. Hussain, F. Conrad and G. R. Patzke, *Angew. Chem., Int. Ed.*, 2009, **48**, 9088; (*c*) W. M. Xuan, A. J. Surman, H. N. Miras, D. L. Long and L. Cronin, *J. Am. Chem. Soc.*, 2014, **136**, 14114; (*d*) J. Y. Niu, K. H. Wang, H. N. Chen, J. W. Zhao, P. T. Ma, J. P. Wang, M. X. Li, Y. Bai and D. B. Dang, *Cryst.*

Growth Des., 2009, **9**, 4362; (*e*) M. K. Saini, R. Gupta, S. Parbhakar, A. K. Mishra, R. Mathurb and F. Hussain, *RSC Adv.*, 2014, **4**, 25357; (*f*) P. Mialane, A. Dolbecq, E. Rivière, J. Marrot and F. Sécheresse, *Eur. J. Inorg. Chem.*, 2004, 33; (*g*) F. Hussain, A. Degonda, S. Sandriesser, T. Fox, S. S. Mal, U. Kortz and G. R. Patzke, *Inorg. Chim. Acta*, 2010, **363**, 4324; (*h*) U. Kortz, *J. Cluster Sci.*, 2003, **14**, 205; (*i*) M. Ibrahim, S. S. Mal, B. S. Bassil, A. Banerjee and U. Kortz, *Inorg. Chem.*, 2011, **50**, 956; (*j*) F. Hussain, R. W. Gable, M. Speldrich, P. Kögerler and C. Boskovic, *Chem. Commun.*, 2009, 328; (*k*) H. Y. An, Z. B. Han and T. Q. Xu, *Inorg. Chem.*, 2010, **49**, 11403; (*l*) C. Ritchie, E. G. Moore, M. Speldrich, P. Kögerler and C. Boskovic, *Angew. Chem., Int. Ed.*, 2010, **49**, 7702; (*m*) S. W. Zhang, Y. Wang, J. W. Zhao, P. T. Ma, J. P. Wang and J. Y. Niu, *Dalton Trans.*, 2012, **41**, 3764; (*n*) P. Mialane, A. Dolbecq, J. Marrot and F. Sècheresse, *Inorg. Chem. Commun.*, 2005, **8**, 740; (*o*) P. Mialane, A. Dolbecq and F. Sécheresse, *Chem. Commun.*, 2006, 3477; (*p*) F. Y. Li, W. H. Guo, L. Xu, L. F. Ma and Y. C. Wang, *Dalton Trans.*, 2012, **41**, 9220; (*q*) K. Wang, D. D. Zhang, J. C. Ma, P. T. Ma, J. Y. Niu and J. P. Wang, *CrystEngComm*, 2012, **14**, 3205; (*r*) Y. Wang, X. P. Sun, S. Z. Li, P. T. Ma, J. P. Wang and J. Y. Niu, *Dalton Trans.*, 2015, **44**, 733; (*s*) W. W. Ju, H. T. Zhang, X. Xu, Y. Zhang and Y. Xu, *Inorg. Chem.*, 2014, **53**, 3269; (*t*) N. Lotfian, M. Mirzaei, H. Eshtiagh-Hosseini, M. Löffler, M. Korabik and A. Salimi, *Eur. J. Inorg. Chem.*, 2014, 5908; (*u*) S. Z. Li, Y. Wang, P. T. Ma, J. P. Wang and J. Y. Niu, *CrystEngComm*, 2014, **16**, 10746; (*v*) Y. Wang, X. P. Sun, S. Z. Li, P. T. Ma, J. Y. Niu and J. P. Wang, *Cryst. Growth Des.*, 2015, **15**, 2057.

6 (*a*) W. L. Chen, Y. G. Li, Y. H. Wang, E. B. Wang and Z. M. Su, *Dalton Trans.*, 2007, 4293; (*b*) X. J. Feng, H. Y. Han, Y. H. Wang, L. L. Li, Y. G. Li and E. B. Wang, *CrystEngComm*, 2013, **15**, 7267; (*c*) C. Ritchie and C. Boskovic, *Cryst. Growth Des.*, 2010, **10**, 488; (*d*) M. Vonci, F. A. Bagherjeri, P. D. Hall, R. W. Gable, A. Zavras, R. A. J. O'Hair, Y. P. Liu, J. Zhang, M. R. Field, M. B. Taylor, J. D. Plessis, G. Bryant, M. Riley, L. Sorace, P. A. Aparicio, X. López, J. M. Poblet, C. Ritchie and C. Boskovic, *Chem. – Eur. J.*, 2014, **20**, 14102; (*e*) C. Ritchie, M. Speldrich, R. W. Gable, L. Sorace, P. Kögerler and C. Boskovic, *Inorg. Chem.*, 2011, **50**, 7004; (*f*) H. Naruke, J. Iijima and T. Sanji, *Inorg. Chem.*, 2011, **50**, 7535; (*g*) Y. J. Liu, H. L. Li, J. L. Zhang, J. W. Zhao and L. J. Chen, *Spectrochim. Acta, Part A*, 2015, **134**, 101.

7 (*a*) F. L. Sousa, A. Ferreira, R. A. S. Ferreira, A. M. V. Cavaleiro, L. D. Carlos, H. I. S. Nogueira, J. Rocha and T. Trindade, *J. Nanosci. Nanotechnol.*, 2004, **4**, 214; (*b*) R. Ballardini, E. Chiorboli and V. Balzani, *Inorg. Chim. Acta*, 1984, **95**, 323; (*c*) N. Haraguchi, Y. Okaue, T. Isobe and Y. Matsuda, *Inorg. Chem.*, 1994, **33**, 1015; (*d*) H. Naruke and T. Yamase, *Bull. Chem. Soc. Jpn.*, 2000, **73**, 375; (*e*) F. L. Sousa, F. A. A. Paz, C. M. C. E. Granadeiro, A. M. V. Cavaleiro, J. Rocha, J. Klinowski and H. I. S. Nogueira, *Inorg. Chem. Commun.*, 2005, **8**, 924; (*f*) D. B. Dang, Y. Bai, C. He, J. Wang, C. Y. Duan and J. Y. Niu, *Inorg. Chem.*, 2010, **49**, 1280.

8 (*a*) M. T. Pope, *Heteropoly and IsopolyOxometalate*, Springer, Berlin, 1983, p. 79; (*b*) G. Hervé and A. C. R. Tézé, *Acad. Sci. Ser. C*, 1974, **278**, 1417.

9 (*a*) A. Tézé, M. Michelon and G. Hervé, *Inorg. Chem.*, 1997, **36**, 505; (*b*) G. M. Maksimov, R. I. Maksimovskaya, G. S. Litvak and J. Russ, *Inorg. Chem.*, 2005, **50**, 1062; (*c*) N. Leclerc-Laronze, J. Marrot, G. Hervé, R. Thouvenot and E. Cadot, *Chem. – Eur. J.*, 2007, **13**, 7234.

10 F. A. Cotton and G. Wilkinson, *Advanced Inorganic Chemistry*, Wiley, New York, 4th edn, 1980, p. 296.

11 (*a*) G. M. Sheldrick, *SHELXS 97, Program for Crystal Structure Solution*, University of Göttingen, Göttingen, Germany, 1997; (*b*) G. M. Sheldrick, *SHELXL 97, Program for Crystal Structure Refinement*, University of Göttingen, Germany, 1997.

12 J. W. Zhao, J. L. Zhang, Y. Z. Li, J. Cao and L. J. Chen, *Cryst. Growth Des.*, 2014, **14**, 1467.

13 (*a*) J. W. Zhao, J. Cao, Y. Z. Li, J. Zhang and L. J. Chen, *Cryst. Growth Des.*, 2014, **14**, 6217; (*b*) L. J. Chen, F. Zhang, X. Ma, J. Luo and J. W. Zhao, *Dalton Trans.*, 2015, **44**, 12598.

14 M. Sadakane, M. H. Dickman and M. T. Pope, *Angew. Chem., Int. Ed.*, 2000, **39**, 2914.

15 K. Suzuki, M. Sugawa, Y. Kikukawa, K. Kamata, K. Yamaguchi and N. Mizuno, *Inorg. Chem.*, 2012, **51**, 6953.

16 S. Reinoso, P. Vitoria, L. S. Felices, L. Lezama and J. M. Gutiérrez-Zorrilla, *Inorg. Chem.*, 2006, **45**, 108.

17 J. W. Zhao, H. L. Li, Y. Z. Li, C. Y. Li, Z. L. Wang and L. J. Chen, *Cryst. Growth Des.*, 2014, **14**, 5495.

18 (*a*) S. Reinoso, M. Giménez-Marqués, J. R. Galán-Mascarós, P. Vitoria and J. M. Gutiérrez-Zorrilla, *Angew. Chem., Int. Ed.*, 2010, **49**, 8384; (*b*) Z. M. Zhang, Y. G. Li, S. Yao and E. B. Wang, *Dalton Trans.*, 2011, **40**, 6475.

19 (*a*) J. Wang, J. W. Zhao, H. Y. Zhao, B. F. Yang, H. He and G. Y. Yang, *CrystEngComm*, 2014, **16**, 252; (*b*) S. Yao, Z. M. Zhang, Y. G. Li, Y. Lu, E. B. Wang and Z. M. Su, *Cryst. Growth Des.*, 2010, **10**, 135; (*c*) C. Ritchie, V. Baslon, E. G. Moore, C. Reber and C. Boskovic, *Inorg. Chem.*, 2012, **51**, 1142.

20 C. H. Li, K. L. Huang, Y. N. Chi, X. Liu, Z. G. Han, L. Shen and C. W. Hu, *Inorg. Chem.*, 2009, **48**, 2010.

21 (*a*) G. Blasse and B. C. Grabmaier, *Luminescent Materials*, Spinger-Verlag, Berlin, 1994; (*b*) L. Armelao, S. Quici, F. Barigelletti, G. Accorsi, G. Bottaro, M. Cavazzini and E. Tondello, *Coord. Chem. Rev.*, 2010, **254**, 487; (*c*) M. D. Allendorf, C. A. Bauer, R. K. Bhakta and R. J. T. Houka, *Chem. Soc. Rev.*, 2009, **38**, 1330.

22 (*a*) Y. Q. Xiao, Y. J. Cui, Q. A. Zheng, S. C. Xiang, G. D. Qian and B. L. Chen, *Chem. Commun.*, 2010, **46**, 5503; (*b*) J. C. Boyer, M. P. Manseau, J. I. Murray and F. C. J. M. van Veggel, *Langmuir*, 2010, **26**, 1157; (*c*) E. Gaidamauskas, H. Parker, B. A. Kashemirov, A. A. Holder, K. Saejueng, C. E. McKenna and D. C. Crans, *J. Inorg. Biochem.*, 2009, **103**, 1652.

23 S. V. Eliseeva and J. C. G. Bunzli, *Chem. Soc. Rev.*, 2010, **39**, 189.

24 (*a*) M. Veith, C. Belot, V. Huch, H. L. Cui, L. Guyard, K. Michael and C. Wickleder, *Eur. J. Inorg. Chem.*, 2010, 879; (*b*) R. M. Abdelhameed, L. D. Carlos, A. M. S. Silva and J. Rocha, *Chem. Commun.*, 2013, **49**, 5019.

25 T. Fujii, K. Kodaira, O. Kawauchi, N. Tanaka, H. Yamashita and M. Anpo, *J. Phys. Chem. B*, 1997, **101**, 10631.

26 E. Cavalli, A. Belletti, R. Mahiou and P. Boutinaud, *J. Lumin.*, 2010, **130**, 733.

27 E. Álvarez, M. E. Zayas, J. Alvarado-Rivera, F. Félix-Domínguez, R. P. Duarte-Zamorano and U. Caldiño, *J. Lumin.*, 2014, **153**, 198.

28 (*a*) B. R. Judd, *Phys. Rev.*, 1962, **127**, 750; (*b*) G. S. J. Ofelt, *Chem. Phys.*, 1962, **37**, 511.

29 (*a*) A. F. Kirby and F. S. Richardson, *J. Phys. Chem.*, 1983, **87**, 2544; (*b*) J. W. Stouwdam and F. C. J. M. van Veggel, *Nano Lett.*, 2002, **2**, 733.

30 T. Zhang, C. Spitz, M. Antonietti and C. F. J. Faul, *Chem. – Eur. J.*, 2005, **11**, 1001.

31 W. T. Xu, Y. F. Zhou, D. C. Huang, W. Xiong, M. Y. Su, K. Wang, S. Han and M. C. Hong, *Cryst. Growth Des.*, 2013, **13**, 5420.

32 S. J. Li, S. X. Liu, N. N. Ma, Y. Q. Qiu, J. Miao, C. C. Li, Q. Tang and L. Xu, *CrystEngComm*, 2012, **14**, 1397.

33 P. Mialane, L. Lisnard, A. Mallard, J. Marrot, E. Antic-Fidancev, P. Aschehoug, D. Vivien and F. Sécheresse, *Inorg. Chem.*, 2003, **42**, 2102.

34 A. Beeby, I. M. Clarkson, R. S. Dickins, S. Faulkner, D. Parker, L. Royle, A. S. deSousa, J. A. G. Williams and M. Woods, *J. Chem. Soc., Perkin Trans. 2*, 1999, 493.

35 (*a*) B. D. Chandler, D. T. Cramb and G. K. H. Shimizu, *J. Am. Chem. Soc.*, 2006, **128**, 10403; (*b*) P. Mahata, K. V. Ramya and S. Natarajan, *Chem. – Eur. J.*, 2008, **14**, 5839.

36 E. G. Moore, A. P. S. Samuel and K. N. Raymond, *Acc. Chem. Res.*, 2009, **42**, 542.

37 Y. Zhang, W. T. Gong, J. J. Yu, H. C. Pang, Q. Song and G. L. Ning, *RSC Adv.*, 2015, **5**, 62527.

38 M. L. Kahn, J. Sutter, S. Golhen, P. Guionneau, L. Ouahab, O. Kahn and D. Chasseau, *J. Am. Chem. Soc.*, 2000, **122**, 3413.

39 Y. Li, F. K. Zheng, X. Liu, W. Q. Zou, G. C. Guo, C. Z. Lu and J. S. Huang, *Inorg. Chem.*, 2006, **45**, 6308.

40 C. Benelli and D. Gatteschi, *Chem. Rev.*, 2002, **102**, 2369.

41 B. Liu, B.-L. Li, Y.-Z. Li, Y. Chen, S.-S. Bao and L.-M. Zheng, *Inorg. Chem.*, 2007, **46**, 8524.

42 Z. H. Zhang, T. Okamura, Y. Hasegawa, H. Kawaguchi, L. Y. Kong, W. Y. Sun and N. Ueyama, *Inorg. Chem.*, 2005, **44**, 6219.

43 C. J. Milios, P. A. Wood, S. Parsons, D. Foguer-Albiol, C. Lampropoulos, G. Christou, S. P. Perlepes and E. K. Brechin, *Inorg. Chim. Acta*, 2007, **360**, 3932.

44 (*a*) F. Ferraro and R. Arratia-Pérez, *Polyhedron*, 2011, **30**, 860; (*b*) V. N. Nikiforov, Y. A. Koksharov, A. V. Gribanov, M. Baran and V. Y. J. Irkhin, *Magn. Magn. Mater.*, 2015, **383**, 215.

45 K. Y. Cui, F. Y. Li, L. Xu, B. B. Xu, N. Jiang, Y. C. Wang and J. P. Zhang, *Dalton Trans.*, 2012, **41**, 4871.

46 T. Arumuganathan and S. K. Das, *Inorg. Chem.*, 2009, **48**, 496.